Observations of an Inertial Peak in the Intrinsic Wind Spectrum Shifted by Rotation in the Antarctic Vortex

L. J. Gelinas[1],
Space Sciences Department, The Aerospace Corporation, El Segundo, CA

R. L. Walterscheid
Space Sciences Applications Laboratory, The Aerospace Corporation, El Segundo, CA

C. R. Mechoso
Department of Atmospheric and Oceanic Sciences, University of California, Los Angeles, CA

G. Schubert
Department of Earth and Space Sciences, University of California, Los Angeles, CA

[1] *Corresponding author address*: Lynette Gelinas, Space Sciences Department, The Aerospace Corporation, PO Box 92957 - M2/260, Los Angeles, CA 90009-2957
E-mail: Lynette.J.Gelinas@aero.org

Abstract

Spectral analyses of time series of zonal winds derived from locations of balloons drifting in the southern hemisphere polar vortex during the VORCORE campaign of the STRATÉOLE program reveal a peak with a frequency near 0.10 hr^{-1}, more than 25% higher than the inertial frequency at locations along the trajectories. Using balloon data and values of relative vorticity evaluated from the Modern Era Retrospective-analyses for Research and Applications (MERRA), we find that the spectral peak near 0.10 hr^{-1} can be interpreted as due to inertial waves propagating inside the Antarctic polar vortex. In support of our claim, we examine the way in which the low-frequency part of the gravity wave spectrum sampled by the balloons is shifted due to effects of the background flow vorticity. Locally, the background flow can be expressed as the sum of solid body rotation and shear. We demonstrate that while pure solid body rotation gives an effective inertial frequency equal to the absolute vorticity, the latter gives an effective inertial frequency that varies, depending on the direction of wave propagation, between limits defined by the absolute vorticity plus or minus half of the background relative vorticity.

1. Introduction

In an atmosphere at rest, the frequency spectrum of internal gravity waves is bounded above by the Brunt-Väisälä frequency and below by the inertial frequency given by the local value of the Coriolis parameter $f = 2\Omega \sin\varphi$, where φ is latitude and Ω is the angular speed of the Earth's rotation (24 hour)$^{-1}$. Inertial gravity waves with lower frequencies are evanescent and have very short attenuation lengths (Eckart 1960).

Atmospheric measurements in Earth-fixed coordinate frames, e.g., time series of stratospheric winds and electric fields, typically show a spectral peak near the inertial frequency (Thompson 1978; Sidi and Barat 1986; Hu and Holzworth 1997). In some cases, however, spectral peaks have been observed at frequencies ~3-20% higher than the inertial frequency. The source of these frequency shifts is not yet fully understood; it has been suggested that Doppler and stratification effects contribute to the shifts (Mori et al. 1990). It has also been suggested that rotational effects originating the vorticity of the background flow might contribute to higher inertial frequencies [Kunze, 1985; Jones 2005; Lee and Eriksen, 1997] and that these effects might be instrumental in trapping near inertial waves in vorticity minima (centers of anticyclonic motion) [Lee and Eriksen, 1997]. Plougonven and Zeitlin [2005] suggest a source of near inertial waves generated by the geostrophic adjustment process.

Shifts in the spectral peak have also been reported in the spectrum of horizontal velocity inferred from location time series of three super-pressure balloons (SPBs) released during the Arctic Kiruna 2002 Campaign (Broutman et al. 2004, Hertzog and Vial 2001). The spectral peak for two of the balloons in that campaign was slightly higher (5-10%) than the inertial frequency (Hertzog et al. 2002). These shifts cannot be due to Doppler effects since measurements made on drifting balloons are recorded in a quasi-Lagrangian reference frame. The spectrum corresponding to a third balloon in the Arctic Kiruna 2002 campaign lacked the near-inertial spectral peak, a feature attributed to differences in the magnitude of meridional excursions, implying significant variations of the Coriolis parameter along that balloon's trajectory.

In the present paper we examine the spectrum of zonal wind speeds derived from location time series of SPBs released in the lower stratosphere during the austral spring of 2005 by the VORCORE Antarctic campaign. One of VORCORE's principal objectives was an improved understanding of the gravity wave field in the Antarctic polar vortex. The SPBs released by VORCORE drifted for several months at two isopycnic levels corresponding approximately to either 50 hPa or 70 hPa. The inertial frequencies corresponding to the latitudes of the SPB locations range from 0.075 hr^{-1} at 65°S to 0.083 hr^{-1} at 90°S (based on $f = 2\Omega \sin\varphi$). However, the data analysis obtains a spectral peak near 0.10 hr^{-1}, more than 25% higher than the largest value of the inertial frequency. We suggest that such a shift to higher frequencies in the spectral peak is consistent with the effects of the relative vorticity of the background flow on the inertial gravity wave field. The effects of the background relative vorticity cannot be ignored in the dispersion relation of the gravity wave field. For example, it has been shown that for some specified configurations of the background flow the lower bound of the inertial wave spectrum is shifted by a substantial fraction of the relative vorticity (Kunze 1985; Kunze and Boss 1998; Jones, 2005). We study these effects for the background flows in which the SPBs drifted during the

VORCORE campaign. Our principal finding is that the spectral peak near 0.10 hr^{-1} can be interpreted as due to inertial waves influenced by the relative vorticity of the background flow inside the Antarctic polar vortex. We show that features of the observed spectra are consistent with relative vorticity expressed as the sum of solid body rotation and shear.

An outline of the paper is as follows. We begin with an overview of the effects of rotation on the gravity wave dispersion relation and the location of the inertial peak (effective inertial frequency). Next, we describe the data sets used, present the results of the data analysis, and compare the observed spectra with the calculated effective inertial frequency which has contributions from both curvature and shear in the vortex. A discussion of the results and limitations of the analysis concludes the paper. A detailed analysis of how relative vorticity influences the effective inertial peak for waves propagating in a rotating and sheared background is given in the appendix.

2. Theory of inertial gravity waves in rotational background flow

In a background state at rest, the approximate dispersion relation for low frequency gravity waves is

$$m^2 = \frac{N^2}{\omega^2 - f^2} k^2 - \frac{1}{4H^2} \qquad (1)$$

Here m is the vertical wavenumber, k is the horizontal wavenumber, ω is wave frequency, N^2 is the square of the Brunt-Väisälä frequency, and H is the scale height. For $\omega < f$, m^2 is less than zero and the wave is evanescent. The inertial-gravity wave spectrum is cut off for frequencies below f.

In a background state not at rest, its effects on the gravity wave dispersion relation are considered in two steps. The first step includes translational effects on wave frequency by replacing ω with the intrinsic frequency $\omega_I = k\left(c - U_k\right)$, where c is the phase speed, k is the magnitude of the horizontal wavenumber vector $\boldsymbol{k}$, and U_k is the component of the background flow projected on $\boldsymbol{k}$. The frequency seen by a drifting balloon is approximately the intrinsic frequency (Hertzog and Vial 2001).

The second step includes rotational effects. This is illustrated for the simple case in which the background velocity field is constant angular velocity $\overline{\Omega} = (\overline{\zeta}/2)\hat{z}$, where $\overline{\zeta}$ is the background vorticity assumed to be constant and $\hat{z}$ is the vertical unit vector around the vertical axis (solid body rotation). In a frame of reference rotating with the flow, and hence with angular velocity $\overline{\Omega} = (\overline{\zeta}/2)\hat{z}$, the horizontal velocity in reference to Earth, $\mathbf{u}$, is given by

$$\mathbf{u} = \mathbf{u}' + \overline{\mathbf{\Omega}} \times \mathbf{r}' \qquad (2)$$

where $\mathbf{u}'$ is the deviation from the background flow, and $\mathbf{r}'$ is the position vector. The fluid acceleration in reference to Earth $d\boldsymbol{u}/dt$ is given by

$$\frac{d\mathbf{u}}{dt} = \frac{\hat{d}\mathbf{u}'}{dt} + 2\overline{\mathbf{\Omega}} \times \mathbf{u}' + \overline{\mathbf{\Omega}} \times \overline{\mathbf{\Omega}} \times \mathbf{r}' \qquad (3)$$

where $\hat{d}\mathbf{u}'/dt$ is the relative acceleration. The second term on the right of (3) is a Coriolis-like term, which in the equations of motion adds to the Coriolis term arising from the rotation of the Earth yielding $\left(f + \overline{\zeta}\right)\hat{\mathbf{z}} \times \mathbf{u}'$. Thus, for such an observer moving with the background flow, such as a drifting balloon, one would have an effective frequency f_{eff} given by

$$f_{eff} = f + \overline{\zeta} \tag{4}$$

To examine how the dispersion relation is changed we consider the equations of motion in the Earth-fixed frame. These are

$$\frac{du}{dt} = \frac{Du}{Dt} - \frac{u\upsilon}{r} = f\upsilon - \frac{1}{\rho}\frac{\partial p}{\partial x} \tag{5}$$

$$\frac{d\upsilon}{dt} = \frac{D\upsilon}{Dt} + \frac{u^2}{r} = -f\,u - \frac{1}{\rho}\frac{\partial p}{\partial y} \tag{6}$$

where $D/Dt = \partial/\partial t + u\,\partial/\partial x + v\,\partial/\partial y + w\,\partial/\partial z$, u, υ and w are, respectively, the azimuthal, radial and vertical components of the velocity, ρ is density and p is pressure. Also, x and y are, respectively, the curvilinear coordinates defined by $dx = rd\theta$ and $dy = dr$, where r , θ and z are, respectively, the radial, azimuthal and vertical coordinates. Let the horizontal background flow be in solid body rotation as above and write the equations of motion for a system rotating with the angular speed of the background flow. The linearized forms of (5) and (6) are

$$\frac{\overline{D}u'}{Dt} + w'\frac{\partial \overline{u}}{\partial z} = (f + 2\overline{\Omega})\upsilon' - \frac{1}{\overline{\rho}}\frac{\partial p'}{\partial x} \tag{7}$$

$$\frac{\overline{D}\upsilon'}{Dt} = -(f + 2\overline{\Omega})u' - \frac{1}{\overline{\rho}}\frac{\partial p'}{\partial y} \tag{8}$$

where $\overline{D}/Dt = \partial/\partial t + \overline{u}\partial/\partial x$, overbars denote the background flow in solid body rotation and primes denote departures therefrom. For this system, the dispersion relation based on the full quasi-static system that includes the heat and continuity equations (see the Appendix) is

$$m^2 = \frac{N^2}{\omega_I^2 - f_{eff}^2} k^2 - \frac{1}{4H^2} \tag{9}$$

where f_{eff} is given by (4), and $\overline{D}/Dt = \omega_I$ where ω_I is the intrinsic frequency.

For $\omega_I{}^2 < f_{eff}^2$, m^2 is negative and the wave is evanescent. Thus the inertial-gravity wave spectrum measured by a balloon is cut off for intrinsic frequencies below the effective inertial frequency.

We show in the appendix that for a more general combination of shear and curvature $\overline{\zeta}_a - \overline{\zeta}/2 \leq f_{eff} \leq \overline{\zeta}_a + \overline{\zeta}/2$, where $\overline{\zeta}_a = f + \overline{\zeta}$ is the absolute vorticity of the background flow. For pure shear (locally approximated as linear shear) with no curvature, wave motion normal to the direction of shear gives $f_{eff} = \overline{\zeta}_a - \overline{\zeta}/2$, while motion along the direction of shear gives $f_{eff} = \overline{\zeta}_a + \overline{\zeta}/2$. When the motion approaches a direction midway between these two extremes $f_{eff} \rightarrow \overline{\zeta}_a$. This is to be compared with the result of Kunze (1985) where $f_{eff} \approx \overline{\zeta}_a - \overline{\zeta}/2$ irrespective of wave direction. Pure solid-body rotation gives $f_{eff} = \overline{\zeta}_a$, in agreement with (5). Accordingly, for measurements made on a balloon drifting with the wind, we expect the spectra derived from an ensemble of waves with a range of directionality to show peak energy between $\omega_I = \overline{\zeta}_a - \overline{\zeta}/2$ and $\omega_I = \overline{\zeta}_a + \overline{\zeta}/2$ rather than near f.

3. Data Description

Beginning on 5 September 2005, the VORCORE campaign released nineteen SPBs with 10 m diameters and eight balloons with 8.5 m diameters from McMurdo, Antarctica (77.5° S, 166.4° E); they drifted near 50 hPa and 70 hPa, respectively. The mean flight duration of the twenty-seven balloons was 59 days and the longest flight duration was 109 days (see Hertzog et al. 2007).

Each SPB carried temperature and pressure sensors and a Global Positioning System (GPS) receiver. Balloon positions were recorded every 15 minutes with a position accuracy of 15 m so that wind speeds could be estimated with accuracy greater than 0.2 m s^{-1} (Hertzog et al. 2007). The geographical sampling of the Antarctic vortex core was very good with best sampling in the 60° S-80° S latitude band and 60° W-120° E longitude sector since the vortex had a tendency to be centered off the pole towards South America (Hertzog et al. 2007).

Evaluation of general conditions in the polar vortex, required to understand and interpret balloon data, was done using the Modern Era Retrospective-analyses for Research and Applications (MERRA) tool produced by NASA. MERRA products are produced at 3 hour intervals with a spatial resolution of ½ degree latitude, 2/3 degree longitude and 72 pressure levels to 0.01 hPa (approximately 80 km altitude). We compute the absolute vorticity using the MERRA horizontal winds to obtain vorticity maps for each 3-hour interval, then interpolate to find the absolute vorticity at the time and location of each balloon measurement. An example vorticity map for 20 October, 2005 derived from MERRA horizontal winds at 52 hPa is presented in the top panel of Figure

1. The values of $\bar{\zeta}$ within the Antarctic polar vortex approach -1 x 10^{-4} s^{-1}, a significant fraction of f (-1.4 x 10^{-4} s^{-1} at 70°S). An example showing the range of absolute vorticity (or effective inertial frequencies assuming pure solid body rotation) inside the vortex is shown in the bottom panel of Figure 1. Inside the vortex, the $|\bar{\zeta}_a|$ is typically ~ 1.8 x 10^{-4} s^{-1}, approximately 25% higher than $|f|$ at these latitudes. Henceforth all references to values of $\bar{\zeta}, \bar{\zeta}_a, f$ and f_{eff}, including minima and maxima are in the sense of the absolute values. Not also that in the following discussion results of the balloon analysis (FFT, wavelet) are given in cycles/s and vorticities in angular frequencies (which include a factor of 2π). This convention is chosen to be consistent with standard practice when discussing vorticity while also allowing intuitive conversion between frequency and period for wave data.

4. Data Analysis and Results

a. Spectral analysis

In this section we present a spectral analysis of zonal wind derived from SPB location data showing a frequency shift of the spectral peak. The SPB flights used in the analysis that follows spanned the October through November period, when, except for late November, the polar vortex remained well-defined and strong. In 2005, the vortex was very stable in September and October, moved off the pole in November and broke up in early December (Hertzog et al. 2007).

Zonal wind velocities were derived from the SPB measurements as described in Hertzog et al. (2007). Fourier analysis of the zonal wind velocity over two-week periods was performed individually for each balloon and then averaged. The results, presented in Figure 2, show a distinct spectral peak at ~0.10 hr^{-1}, well separated from the frequency of the semidiurnal tide (indicated by the green line), that persists from early October through November. The red hatched area shows the range of inertial frequencies *f* for all balloons in the two week period; effective inertial frequencies for pure solid body rotation, $f_{eff} = \overline{\zeta}_a$, for each two-week period are indicated by the black hatched area in Figure 2. For each two-week period considered, the spectral peak falls within the range of solid-body effective inertial frequencies, and generally lies outside the range of the frequencies found for *f*. The peak shifts toward the inertial frequency range in late December, which is consistent with the breakup of the vortex.

b. Wavelet Analysis

The intermittent nature of inertial waves suggests wavelet analysis as a means to explore the temporal behavior of the zonal wind spectra. The time series from each balloon was analyzed with Morlet wavelets in order to identify the spectral features as a function of time (Torrence and Compo 1998). The wavelet analysis confirmed that the dominant peak in the spectrum occurred near 0.1 hr^{-1}, as indicated by the Fourier analysis discussed above. The peak wavelet power was generally found to lie between ~0.08 – 0.13 hr^{-1}.

Figure 3 shows the results of a wavelet analysis for three sample balloon trajectories. Also shown are the values of the inertial frequency at the balloon location *f* and the local value of $\overline{\zeta}_a$ (f_{eff} for the case of pure solid body rotation). Local values of $\overline{\zeta}_a$ are determined by interpolating MERRA vorticity to each balloon trajectory as a function of location and time at the 52 hPa pressure level. Figure 3 shows that there is significantly better agreement between the location of the spectral peak and $\bar{\zeta}_a$ (black curves), than the frequency corresponding to *f* (red curves), particularly in October and early November. Several instances of significant spectral peaks on the low frequency side of f_{eff} seen in Balloon 2 during November, when a significant oscillation occurs near 20 hours (the lowest plotted frequency), is probably a manifestation of the diurnal tide.

There are a number of instances in Figure 3 for which a cutoff near $\bar{\zeta}_a$ is not apparent. Results of a statistical analysis to examine the difference between the frequency of the measured spectral peak and the local values of *f* are presented in Figure 4. The frequency of maximum wavelet power is determined for each balloon measurement, e.g., the frequency of the peak wavelet power as a function of time for the wavelet spectra shown in Figure 3. The results, binned in 0.05 s^{-1} intervals, are presented in Figure 4, which shows the number of balloon measurements as a function of difference between measured peak frequency f_m and inertial frequency *f*. Note that wave period, rather than frequency, is plotted since the wavelet algorithm used for the spectral analysis returns wavelet power as a function of period rather than frequency and is the natural way to bin the results. Statistics are presented for each two-week period in October and November, since the wavelet analysis shown in Figure 3 suggests that the spectral peak diverges from pure solid body rotation $f_{eff} = \bar{\zeta}_a$ sometime in November.

The distribution of balloon measurements presented in Figure 4 shows peaks near ζ_a as well as peaks displaced somewhat from $\bar{\zeta}_a \pm \bar{\zeta}/2$ toward $\bar{\zeta}_a$. The spectral peak of zonal wind measurements for October is generally consistent with that expected for pure solid body rotation $\bar{\zeta}_a$ with secondary contributions near $\bar{\zeta}_a \pm \bar{\zeta}/2$. The vortex was observed to weaken, deform and move off the pole during November. The main peak in the occurrence frequency shifts toward $\bar{\zeta}_a - \bar{\zeta}/2$ in the first half of November and in the second half the main part of the distribution is found between $\bar{\zeta}_a - \bar{\zeta}/2$ and $\bar{\zeta}_a$ with a slight bias toward $\bar{\zeta}_a - \bar{\zeta}/2$. In section 5 it is shown that the relative vorticity can be expressed as the sum of a solid body component and a shear component. The displacement away from $\bar{\zeta}_a$ is consistent with an increase in the relative contribution of the non-solid body component. The high-frequency tail is associated with power from sporadic high-frequency gravity waves that occasionally cause peak amplitudes at frequencies higher than the inertial frequency, and is consistent with the results from the Fourier analysis presented earlier in Figure 2.

5. Discussion

We show in the appendix that for a fairly general combination of shear and rotation $\bar{\zeta}_a - \bar{\zeta}/2 \le f_{eff} \le \bar{\zeta}_a + \bar{\zeta}/2$, where $\bar{\zeta}_a = f + \bar{\zeta}$ is the absolute vorticity of the background state. In a "natural" coordinate system where the x-axis is along the basic flow velocity vector and the y-axis is in the orthogonal direction consistent with a right-handed system the vorticity is written (Holton, 1972)

$$\bar{\zeta} = U\frac{\partial \beta}{\partial s} - \frac{\partial U}{\partial y} \tag{10}$$

where $\partial\beta/\partial s$ is the rate of change of the angle β between the x-axis and the tangent to the streamline as a function of the distance s along the streamline. In terms of the local radius of curvature r

$$\overline{\zeta} = \frac{U}{r} - \frac{\partial U}{\partial y} \tag{11}$$

where r is positive for cyclonic motion and U is the velocity component in the x-direction.

Since the horizontal scale k^{-1} of typical gravity waves (~a few tens of kilometers or less) is much less than the scale of variation of the background flow (~ a few hundred kilometers or more) we can expand the wind field to first order using a Taylor expansion of the rotational part of the wind field at the balloon position as $U_\zeta\left(y\right) = U_0 + Ay$ and $V_\zeta\left(x\right) = Bx$, whence

$$\overline{\zeta} = B - A \tag{12}$$

When $A = -a$ and $B = a$ one obtains the result for solid body rotation $\overline{\zeta} = 2a$ (see Appendix). In terms of (11), $a = \left(U/r\right)_0$ and $\overline{\zeta} = 2\left(U/r\right)_0$. More generally we can write $A = a + \delta a$ and express (11) in terms of the sum of vorticity from solid body rotation and the excess shear in addition to the shear that is consistent with solid body rotation as follows

$$\overline{\zeta} = 2\frac{U}{r} + \delta\overline{\zeta} \tag{13}$$

where $\delta\overline{\zeta} = -\delta a = -\left(U/r + \partial U/\partial y\right)_0$.

In the appendix we show that for pure shear with no curvature, wave motion normal to the direction of shear gives $f_{eff} = \overline{\zeta}_a - \overline{\zeta}/2$, while wave motion along the direction of shear gives $f_{eff} = \overline{\zeta}_a + \overline{\zeta}/2$. When the wave motion approaches a direction midway between these two extremes $f_{eff} \rightarrow \bar{\zeta}_a$. This is to be compared with the result of Kunze (1985) where $f_{eff} \approx \bar{\zeta}_a - \bar{\zeta}/2$, irrespective of the direction of wave motion. Pure solid body rotation gives $f_{eff} = \bar{\zeta}_a$ in agreement with (4). Accordingly, for measurements made on a balloon drifting with the wind, we expect the spectra derived from an ensemble of waves with a range of directionality to show peak energy between $\omega_I = \bar{\zeta}_a - \bar{\zeta}/2$ and $\omega_I = \bar{\zeta}_a + \bar{\zeta}/2$ rather than near *f*.

An example of the relative contribution from solid-body rotation and shear excess is presented for 20 October, 2005 in Figure 5. The total vorticity for this date was depicted previously in Figure 1. The top two panels of Figure 5 show the curvature and shear vorticity, U/r and $\partial U/\partial y$, respectively, as discussed earlier in this section. The contribution from solid body rotation $2U/r$ is shown in the lower left panel of Figure 5 and the excess shear vorticity $-(\partial U/\partial y + U/r)$ in the lower right panel. Clearly, on this date the dominant component of the relative vorticity is from solid body rotation, which suggests an effective inertial frequency near $\bar{\zeta}_a$.

The temporal change of the effective inertial frequency depicted in Figure 4 suggests that the relative contributions of solid body and shear vorticity change between the October and November observation periods. A statistical analysis of the ratio of the solid body to shear vorticity for each two week time period is presented in Figure 6. Solid body and shear vorticity were calculated from MERRA data, and then interpolated to the balloon locations. Figure 6 shows the percentage of balloon measurements having the indicated solid body to shear vorticity ratio. The solid body component clearly dominates throughout October, where nearly 14% of the balloon observations showed dominant solid body rotation, as compared to approximately 4% of observations for which the shear component of the vorticity dominates. From this, it would be expected that the main peak in the occurrence frequency for the effective inertial frequency for October would be shifted only slightly off $\bar{\zeta}_a$, as is shown in Figure 4. The existence of two dominant peaks, one centered near zero and the other near -2, is informative. The first peak is consistent with large shear and negligible curvature. These conditions can exist near the boundaries of a vortex where, even though the curvature may not be small, the shear may be very large in comparison (see Figure 5). The second peak corresponds to negligible excess shear. These conditions are consistent with conditions that cover more extensive areas in the central part of the vortex.

By the end of November, however, the relative contributions of solid body and shear vorticity are nearly equal, with the average value of the effective inertial frequency expected to be shifted away from $\bar{\zeta}_a$ toward either $\bar{\zeta}_a - \bar{\zeta}/2$ or $\bar{\zeta}_a + \bar{\zeta}/2$ depending on wave directionality. The statistics presented in Figure 4 show that the former is favored. The results presented in Figure 4 suggest that a large fraction of the waves measured by the balloons are propagating in a direction not too different from that of the wind. The shift toward $\bar{\zeta}_a - \bar{\zeta}/2$ is consistent with the wavenumber vector aligned with the wind in laterally sheared flow, such as near the boundaries of the vortex. An inspection of the balloon trajectories indicates that balloons tend to be found near the vortex boundary much of the time in late November. These comparisons show that the solid-body rotation component dominates the absolute vorticity for much of October, but by early November the excess shear component becomes stronger as the vortex deforms and weakens.

6. Summary and conclusions

We have applied spectral methods to analyze wind fields from SPB measurements, and used vorticity fields from the MERRA analysis to identify and interpret spectral features of low-frequency inertial gravity waves recorded by VORCORE balloons in the Antarctic stratosphere. Balloon spectra were derived using both Fourier and wavelet analyses. We have shown that the spectral peak of wind measurements made on balloons drifting with the wind is shifted to frequencies more than 25% higher than the local inertial frequency. Frequency shifts have been reported in other works but were either made in a non-intrinsic frame (Mori et al., 1990) or showed significantly smaller shifts (Hertzog et al., 2002). The exceptionally strong Antarctic polar vortex allowed identification of the peak as that corresponding to a shift in the inertial frequency f (Coriolis parameter) by the relative vorticity $\overline{\zeta}$. We interpret f_{eff} as the inertial frequency in a coordinate frame moving with the basic flow.

We study the case in which the flow locally can be written as the superposition of solid body rotation and simple shear. The solid body contribution gives $f_{eff} = f + \overline{\zeta}$ independent of wave directionality. The shear contribution gives values $\overline{\zeta}_a - \frac{1}{2}\overline{\zeta} \le f_{eff} \le \overline{\zeta}_a + \frac{1}{2}\overline{\zeta}$ depending on wave direction. Our observations are consistent with a spectrum of waves contributing to a spread of f_{eff}, with the distribution broadly consistent with $f_{eff} \approx \overline{\zeta}_a$ during October and early November, but peaked closer to $f_{eff} \approx \overline{\zeta}_a - \frac{1}{2}\overline{\zeta}$ in late November as the vortex weakened.

A possible source for a peak at frequencies higher than f is waves generated by fronts and jets. These waves have frequencies near 1.4 f [O'Sullivan and Dunkerton, 1995; Plougonven and Snyder 2005a,b]. However these frequencies are significantly higher than the inertial peak we observe. We have examined the possibility that the 0.1 hr^{-1} peak is representative of the semidiurnal tide Doppler shifted by balloon motion, but found this effect to be too small to account for the observed shift. Nor do we find the large-scale coherency expected for a tide. Finally, we have examined pressure variations and find minimal power in the 0.08-0.12 hr^{-1} band (not shown here). This is a characteristic feature of inertial waves.

Acknowledgments

The authors especially thank Andrew V. Tangborn, from the National Aeronautics and Space Administration, for providing the GEOS5 data. The VORCORE data were provided by the France's Centre National de la Recherche Scientifique from their web site http://www.lmd.polytechnique.fr/VORCORE/McMurdoE.htm. Research at The Aerospace Corporation and UCLA was supported by NSF Grant ATM – 0732222. Research at The Aerospace Corporation was also supported by NASA Grant NNX08AM13G.

APPENDIX

In this appendix we derive expressions for the inertial frequency in a flow combining rotation and linear shear. The latter should give a reasonable representation of the shear experienced by inertial gravity waves in a slowly spatially varying background wind field. We show that depending on the flow configuration and wave directionality $f_{eff} = \bar{\zeta}_a + \frac{1}{2} n\bar{\zeta}$, where $n = -1, 0, 1$ and where $\bar{\zeta}_a = f + \bar{\zeta}$ is the absolute vorticity. Before we proceed to consider inertia gravity waves in a stratified atmosphere we consider the simple case of solid body rotation for pure inertial waves in Cartesian geometry.

1. Inertial waves in solid body rotation (Cartesian formulation)

In Cartesian coordinates cyclonic solid body rotation is given by $U(y) = U_0 - ay$ and $V(x) = V_0 + ax$, where $\mathbf{U} = (U, V)$ is the basic horizontal flow. Pure inertial motion on a background state in solid body rotation is given by

$$\begin{aligned} &\frac{\partial u'}{\partial t} + U\frac{\partial u'}{\partial x} + V\frac{\partial u'}{\partial y} - (a+f)v' = 0 \\ &\frac{\partial v'}{\partial t} + U\frac{\partial v'}{\partial x} + V\frac{\partial v'}{\partial y} + (a+f)u' = 0 \end{aligned} \tag{1.1}$$

This generates the vorticity equation

$$\frac{\bar{D}\zeta'}{Dt} + (f + \bar{\zeta})\delta' = 0 \tag{1.2}$$

and the divergence equation

$$\frac{\bar{D}\delta'}{Dt} - (f + \bar{\zeta})\zeta' = 0 \tag{1.3}$$

where $\zeta = -\partial u/\partial y + \partial v/\partial x$, $\delta = \partial u/\partial x + \partial v/\partial y$,

$$\frac{\bar{D}}{Dt} = \frac{\partial}{\partial t} + U\frac{\partial}{\partial x} + V\frac{\partial}{\partial y} \tag{1.4}$$

and $\bar{\zeta} = 2a$. Elimination of the divergence between (2) and (3) gives

$$\frac{\bar{D}^2\zeta'}{Dt^2}+\left(f+\bar{\zeta}\right)^2\zeta'=0 \qquad (1.5)$$

whence

$$\omega_I^2=\left(f+\bar{\zeta}\right)^2 \qquad (1.6)$$

or $f_{eff}=f+\bar{\zeta}=\bar{\zeta}_a$.

This agrees with the results obtained in section 4.

Note that in deriving (4) we assumed that the advective terms in (1.2) and (1.3) were locally constant. This differs from assuming that the advective terms are locally constant from the onset (Kunze , 1985). It is instructive to look at the vorticity equation when the advective terms in (1.1) are forced to be constant. One then obtains the incorrect result

$$\frac{\bar{D}\zeta'}{Dt}+\left(f+\bar{\zeta}/2\right)\delta'=0 \qquad (1.7)$$

This example shows that when considering a system where rotational effects are important it is essential to work with equations that preserve the correct form of the vorticity equation. It also shows that assuming that the advection terms are locally constant in the divergence and vorticity equations (1.2) gives the correct result $f_{eff}=f+\bar{\zeta}$.

2. Inertial gravity waves

We work with the vorticity and divergence equations in lieu of the horizontal momentum equations for the reasons discussed in the previous section. The equations in the log-pressure system are (Andrews et al., 1987).

$$\frac{\bar{D}\zeta'}{Dt} + \left(f + \bar{\zeta}\right)\delta' = 0 \tag{2.1}$$

$$\frac{\bar{D}\delta'}{Dt} - 2\bar{\zeta}\frac{\partial v'}{\partial x} - f\zeta' = -\nabla^2\varphi' \tag{2.2}$$

$$\frac{\partial w'}{\partial z} - w' + \delta' = 0 \tag{2.3}$$

$$\frac{\bar{D}}{Dt}\frac{\partial \varphi'}{\partial z} + Sw' = 0 \tag{2.4}$$

where $z = -\log\left(p/p_0\right)$, $w = \dot{z}$, $S = RT\log\bar{\theta}/dz$, and $\phi' = g\eta'$ and where η' is the disturbance height of pressure surfaces.

Let the velocity be written in terms of the stream function ψ and velocity potential χ, whence

$$u' = -\frac{\partial \psi'}{\partial y} + \frac{\partial \chi'}{\partial x} \tag{2.5}$$

$$v' = \frac{\partial \psi'}{\partial x} + \frac{\partial \chi'}{\partial y} \tag{2.6}$$

This gives

$$\frac{\bar{D}\nabla^2\psi'}{Dt} + \left(f + \bar{\zeta}\right)\nabla^2\chi' = 0 \tag{2.7}$$

$$\frac{\bar{D}\nabla^2\chi'}{Dt} - 2\bar{\zeta}\frac{\partial}{\partial x}\left(\frac{\partial \psi'}{\partial x} + \frac{\partial \chi'}{\partial y}\right) - f\nabla^2\psi' = -\nabla^2\varphi' \tag{2.8}$$

$$\frac{\partial w'}{\partial z} - w' + \nabla^2\chi' = 0 \tag{2.9}$$

To transform out the exponential growth with altitude one defines a new set of variables

$$\xi' = \hat{\xi}\exp(z/2) \tag{2.10}$$

where ξ is any dependent variable. Then (2.9) becomes

$$\left(\frac{\partial}{\partial z} - \tfrac{1}{2}\right)\hat{w} + \nabla^2 \hat{\chi} = 0 \tag{2.11}$$

and (2.4) becomes

$$\frac{\bar{D}}{Dt}\left(\frac{\partial}{\partial z} + \frac{1}{2}\right)\hat{\varphi} + S\hat{w} = 0 \tag{2.12}$$

otherwise one simply replaces primes with carets in (2.7) and (2.8).

To obtain a dispersion relation we eliminate $\hat{\psi}$ in favor of $\hat{\chi}$ using (7), eliminate $\hat{\chi}$ in favor of $\hat{w}$ using (2.11) and finally eliminate $\hat{\varphi}$ in favor of $\hat{w}$ using (2.12). Assuming solutions of the form

$$\left(\frac{\partial}{\partial x}, \frac{\partial}{\partial x}, \frac{\partial}{\partial x}, \frac{\bar{D}}{Dt}\right) = \left(-ik, -il, -im, i\omega_I\right) \tag{2.13}$$

where *m* is the nondimensional vertical wavenumber in the log-pressure system gives the dispersion relation

$$m^2 = \frac{Sk_H^2}{\omega_I^2 - \left(f + \bar{\zeta}\right)^2 - \bar{\zeta}\left(f + \bar{\zeta}\right)\left(k^2 - l^2\right) / k_H^2 + i2\omega_I \bar{\zeta}\, kl / k_H^2} - \frac{1}{4} \tag{2.14}$$

where $k_H^2 = k^2 + l^2$. We have assumed that $\bar{\delta} = 0$. For low-frequency waves for which $m^2 >> 1$, (2.14) may be written

$$m^2 = \frac{Sk_H^2}{\omega_I^2 - \left(f+\bar{\zeta}\right)^2 - \bar{\zeta}\left(f+\bar{\zeta}\right)\left(k^2-l^2\right)\big/k_H^2 + i2\omega_I\bar{\zeta}\,kl\big/k_H^2} \tag{2.15}$$

The denominator in (2.14) and (2.15)

$$\Delta = \omega_I^2 - \left(f+\bar{\zeta}\right)^2 - \bar{\zeta}\left(f+\bar{\zeta}\right)\left(k^2-l^2\right)\big/k_H^2 + i2\omega_I\bar{\zeta}\,kl\big/k_H^2 \tag{2.16}$$

is just the dispersion relation for pure inertial waves when $\Delta = 0$. This justifies the simpler treatment when Δ is real. When Δ is complex we need the full dispersion relation to interpret what this means (it does not mean that ω_I is complex).

3. Inertial gravity waves in linear shear

As in section 4, we approximate the shear over the dimensions of a pure inertial wave in terms of linear shear. Let $U(y) = U_0 + ay$ and $V(y) = V_0$, where U_0 and V_0 are constants, then

$$\begin{aligned} &\frac{\bar{D}u'}{Dt} - (f-a)v' = 0 \\ &\frac{\bar{D}v'}{Dt} + f\,u = 0 \end{aligned} \tag{3.1}$$

The vorticity equation is

$$\frac{\bar{D}\zeta'}{Dt} + \left(f+\bar{\zeta}\right)\delta' = 0 \tag{3.2}$$

The divergence equation is (Salmon, 1998)

$$\frac{\bar{D}\delta'}{Dt} - 2J(u,v) - f\zeta' = 0 \tag{3.3}$$

The linearized Jacobian is

$$J\left(u,v\right)=-\frac{\partial}{\partial y}\left(u'+U\right)\frac{\partial}{\partial x}\left(v'+V\right)=-\frac{\partial U}{\partial y}\frac{\partial v'}{\partial x}=\overline{\zeta}\,\frac{\partial v'}{\partial x} \tag{3.4}$$

Using (3.4) in (3.3) gives

$$\frac{\overline{D}\delta'}{Dt}-2\overline{\zeta}\,\frac{\partial v'}{\partial x}-f\zeta'=0 \tag{3.5}$$

We consider three special cases, viz., $\theta=0,\ \pi/4,\ \pi/2$ corresponding to l=0, k=l and k=0.

3.1. PROPAGATION NORMAL TO THE SHEARED DIRECTION

With $\partial/\partial y=-il=0$, $\zeta'=\partial v'/\partial x$, and (3.5) becomes

$$\frac{\overline{D}\delta'}{Dt}-\left(f+2\overline{\zeta}\right)\zeta'=0 \tag{3.6}$$

Eliminating the divergence between (3.2) and (3.6) gives

$$f_{eff}=\sqrt{\left(f+\overline{\zeta}\right)\left(f+2\overline{\zeta}\right)}\approx\left(f+\overline{\zeta}\right)+\tfrac{1}{2}\overline{\zeta} \tag{3.7}$$

This agrees with (2.16) with $l=0$ and $\Delta=0$.

3.2. PROPAGATION ALONG THE SHEARED DIRECTION

With $\partial/\partial x=-ik=0$, (3.5) becomes

$$\frac{\overline{D}\delta'}{Dt}-f\zeta'=0 \tag{3.8}$$

Eliminating the divergence between (3.2) and (3.8) gives

$$f_{eff}=\sqrt{f\left(f+\overline{\zeta}\right)}\approx\left(f+\overline{\zeta}\right)-\tfrac{1}{2}\overline{\zeta} \tag{3.9}$$

This agrees with (2.16) with $k=0$ and $\Delta=0$.

3.3. PROPAGATION AT 45° TO THE SHEARED DIRECTION

For this case we use the more general theory for inertial gravity waves for the same basic state linear shear. Equation (2.16) may be rewritten in terms of wave direction as

$$\Delta = \omega_I^2 - \left(f + \bar{\zeta}\right)^2 + \bar{\zeta}\left(f + \bar{\zeta}\right)\cos 2\theta + i\omega_I \bar{\zeta}\sin 2\theta \qquad (3.10)$$

where θ is the direction of propagation with respect to the x-axis (i.e., $\cos\theta = k/k_H$). Propagation midway between propagation along and normal to the shear ($l = k$) gives

$$\Delta = \omega_I^2 - \left(f + \bar{\zeta}\right)^2 + i\omega_I \bar{\zeta} \qquad (3.11)$$

In this case there is no singularity (value of ω_I for which $\Delta = 0$), rather there is a minimum where the real part of m maximizes. The real part of m may be written as

$$m_r = \frac{-S^{\frac{1}{2}} k_H}{\left[\left(\omega_I^2 - \bar{\zeta}_a^2\right)^2 + \omega_I^2 \bar{\zeta}^2\right]^{\frac{1}{4}}} \cos\left(\alpha/2\right) \qquad (3.12)$$

where $\alpha = \tan^{-1}\left(\omega_I \bar{\zeta} / \left(\omega_I^2 - \bar{\zeta}_a^2\right)\right)$ and the minus sign is chosen to give upward energy propagation. The maximum absolute value of m_r occurs for $\omega_I = \bar{\zeta}_a$ and

$$m_r = \frac{-S^{\frac{1}{2}} k_H}{\sqrt{\bar{\zeta}_a \bar{\zeta}}} \cos\left(\pi/4\right) \qquad (3.13)$$

For reasonable background values $m_r \sim 2\times 10^2$ corresponding to very short vertical wavelengths (a small fraction of a scale height). Such short wavelength near inertial waves would almost certainly be absorbed by scale dependent diffusion (i.e., cutoff).

3.4. RELATION TO SOLID BODY ROTATION

Solid body rotation gives wave propagation in flow that is simultaneously sheared along and normal to the direction of propagation. If one averages the contribution from each direction using (3.7) and (3.9) one obtains $f_{eff} = f + \bar{\zeta}$, in agreement with the known result (see (1.6)).

3.5 RELATION TO APPROACH OF KUNZE (1985)

Kunze (1985) considered inertial gravity waves in sheared flow and obtained the result $f_{eff} \approx f + \bar{\zeta}/2$. The basic approach was to derive the dispersion relation by assuming at the onset that the advection terms were locally constant. We have seen that for solid body rotation this gives the result $f_{eff} = f + \bar{\zeta}/2$ when the known result is $f_{eff} = f + \bar{\zeta}$. For propagation normal to the shear the approach of Kunze (1985) gives

$$\frac{\bar{D}\delta'}{Dt} - \bar{\zeta}\frac{\partial v'}{\partial x} - f\zeta' = 0 \qquad (3.10)$$

Whence $f_{eff} = \sqrt{f\left(f + \bar{\zeta}\right)} \approx f + \frac{1}{2}\bar{\zeta}$ in contrast to (3.7). For propagation along the shear the approach of Kunze (1985) also gives $f_{eff} \approx f + \bar{\zeta}/2$ in agreement with (3.9). As we have argued, solid body rotation is the average of the contributions from the shear in each direction. Thus the incorrect result for solid body rotation is consistent with the result $f_{eff} \approx f + \bar{\zeta}/2$ obtained independent of whether the direction of propagation is normal to or along the sheared direction.

References

Andrews, D. G., J. R. Holton, and C. B. Leovy, 1987: *Middle Atmosphere Dynamics, Academic Press*, 489 pp.

Broutman D., R. H. J. Grimshaw, and S. D. Eckermann, 2004: Internal waves in a Lagrangian reference frame, *J. Atmos. Sci.,* **61**, 1308-1313.

Eckart, C., *Hydrodynamics of Oceans and Atmospheres*, Pergamon Press, New York, 290 pp, 1960.

Hertzog, A, and F. Vial, 2001: A study of the dynamics of the equatorial lower stratosphere by use of ultra-long duration balloon, 2. Gravity waves, *J. Geophys. Res.,* **106**, 22,745 – 22,761.

Hertzog, A., Vial, F., Mechoso, C.R., Basdevant, C., and P. Cocquerez, 2002: Quasi-Lagrangian measurements in the lower stratosphere reveal an energy peak associated with near-inertial waves, *Geophys. Res. Lett*., **29 (8)**, 70-74.

Hertzog A. P. Cocquerez, C. Basdevant, G. Boccara, J. Bordereau, B. Brioit, A. Cardonne, R. Guilbon, A. Ravissot, É. Schmitt, J.-N. Valdivia, S. Venel, and F. Vial, 2007: Stratéole/Vorcore -Long-duration, superpressure balloons to study the Antarctic lower stratosphere during the 2005 winter, *J. Atmos. Ocean. Technol.***, 24**, 2048-2061.

Holton, J. R., 1972: *An Introduction to Dynamic Meteorology*, Academic Press, 319 pp.

Hu, H., and R. H. Holzworth, 1997: An inertial wave-driven stratospheric horizontal electric field: New evidence, *J. Geophys. Res.,* **102*(D16)*,** 19,717–19,727.

Jones, R.M., 2005: A general dispersion relation for internal gravity waves in the atmosphere or ocean, including baroclinicity, vorticity, and rate of strain, *J. Geophys. Res.,* **110**, D22106, doi:10.1029/2004JD005654.

Lee C.M. and C.C. Eriksen,1997:, Near-inertial internal wave interactions with mesoscale fronts: observations and models, *J. Geophys. Res.* **102**, 3237-3253.

Kunze, E. ,1985: Near-inertial wave propagation in geostrophic shear, *J. Phys. Ocean.,* **15**, 544-564.

Kunze, E., and E. Boss, 1998: A model for vortex-trapped internal waves, *J. Phys. Ocean.,* **28**, 2104-2115.

Mori, Y. ,1990: Evidence of inertial oscillations of the surface wind at Marcus Island, *J. Geophys. Res.*, **95(D8)**, 11,777–11,783.

Plougonven, R., and C. Snyder, 2005a: Gravity waves excited by jets: Propagation versus generation. Geophys. Res. Lett., 32, L18892, doi:10.1029/2005GL023730

Plougonven, R., and C. Snyder, 2007b: Inertia–Gravity Waves Spontaneously Generated by Jets and Fronts. Part I: Different Baroclinic Life Cycles. *J. Atmos. Sci.,* **64**, 2502-2520, DOI: 10.1175/JAS3953.1

Plougonven R. and V. Zeitlin, 2005: Lagrangian approach to the geostrophic adjustment of frontal anomalies in a stratified fluid. *Geophysical and Astrophysical Fluid Dynamics, 99*, 101-135, DOI: 10.1080/03091920512331328080.

O'Sullivan, D., and T. J. Dunkerton, 1995: Generation of inertia– gravity waves in a simulated life cycle of baroclinic instability. *J. Atmos. Sci.,* **52**, 3695–3716.

Rienecker, M. M., M. J. Suarez, R. Todling, J. Bacmeister, L. Takacs, H.-C. Liu, W. Gu, M. Sienkiewicz, R. D. Koster, R. Gelaro, I. Stajner, and E. Nielsen , 2008: The GEOS-5 Data Assimilation System - Documentation of Versions 5.0.1, 5.1.0, and 5.2.0. *Technical Report Series on Global Modeling and Data Assimilation 104606*, v27.

Sidi, C., and J. Barat, 1986: Observational evidence of an inertial wind structure in the stratosphere, *J. Geophys. Res.,* **91(D1)**, 1209–1217.

Salmon, R., 1998: *Lectures on Geophysical Fluid Dynamics*, Oxford University Press, 378 pp.

Tangborn. A, 2008: BIRS Data Assimilation Workshop, Banff, Canada. February 3-8, 2008, http://www.atmos.ucla.edu/~kayo/birs/pdf/tangborn_birs_da08.pdf

Thompson, R. O. R. Y. , 1978: Observation of inertial waves in the stratosphere, *Q. J. R. Meteorol. Soc.*, **104**, 691–698.

Torrence, C. T. and G.P. Compo, 1998: A practical guide to wavelet analysis, *Bull. Amer. Meteor. Soc.,* **71**, 61-78.

List of Figures

Figure. 1. Relative and absolute vorticity at 52 hPa calculated using MERRA data for October 20, 2005.

Figure 2. Average power spectra from Fourier analysis of zonal winds. Each panel shows the average of individual balloon spectra in a 2-week period (black line). The red-hatched region shows the range of inertial frequencies f for all balloons in flight during the 2-week window. The black-hatched region shows the range of absolute vorticity $\bar{\zeta}_a$ in each two-week period. The green line indicates the semidiurnal tide, which appears in mid-November.

Figure 3. Wavelet spectra for balloons 1, 2 and 8, released near 50 hPa. Inertial frequency f (a function only of latitude) is shown in red for each balloon trajectory. The absolute vorticity (a function of latitude and relative vorticity) is shown as a solid black line.

Figure 4. Statistical analysis of the occurrence frequency of inferred differences between the frequency of the measured spectral peak (f_m) and the inertial frequency (f). Values are shown for successive two-week periods in October and November. Peaks are observed near $\bar{\zeta}_a = f + \bar{\zeta}$ and between $\bar{\zeta}_a$ and $\bar{\zeta}_a \pm \bar{\zeta}/2$.

Figure 5. The top two panels show maps of the curvature and shear vorticity, U/r and $\partial U/\partial y$, respectively (see text). The contribution from solid body rotation $2U/r$ is shown in the lower left panel and the non-solid body shear vorticity $-\left(\partial U/\partial y + U/r\right)$ defined in (13) is shown in the lower right panel.

Figure 6. Statistical analysis of the occurrence frequency of the solid body to shear ratio for each two-week period of balloon measurements (See Figure 4).

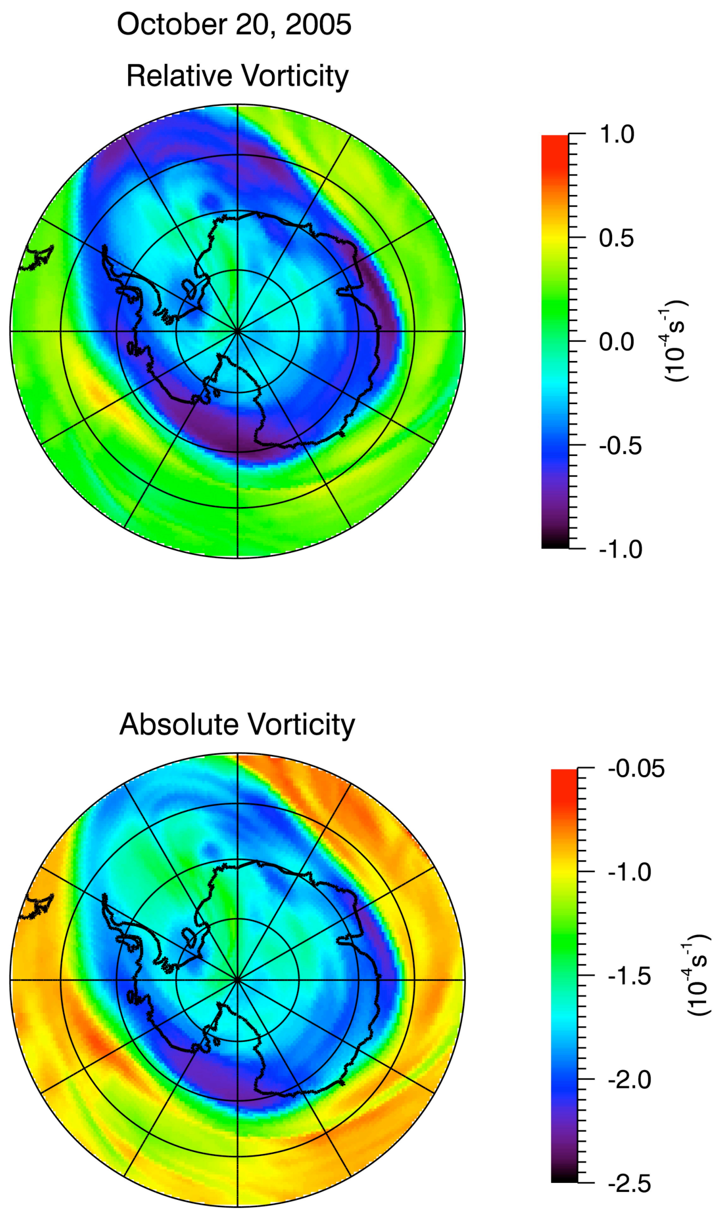

Figure. 1. Relative and absolute vorticity at 52 hPa calculated using MERRA data for October 20, 2005.

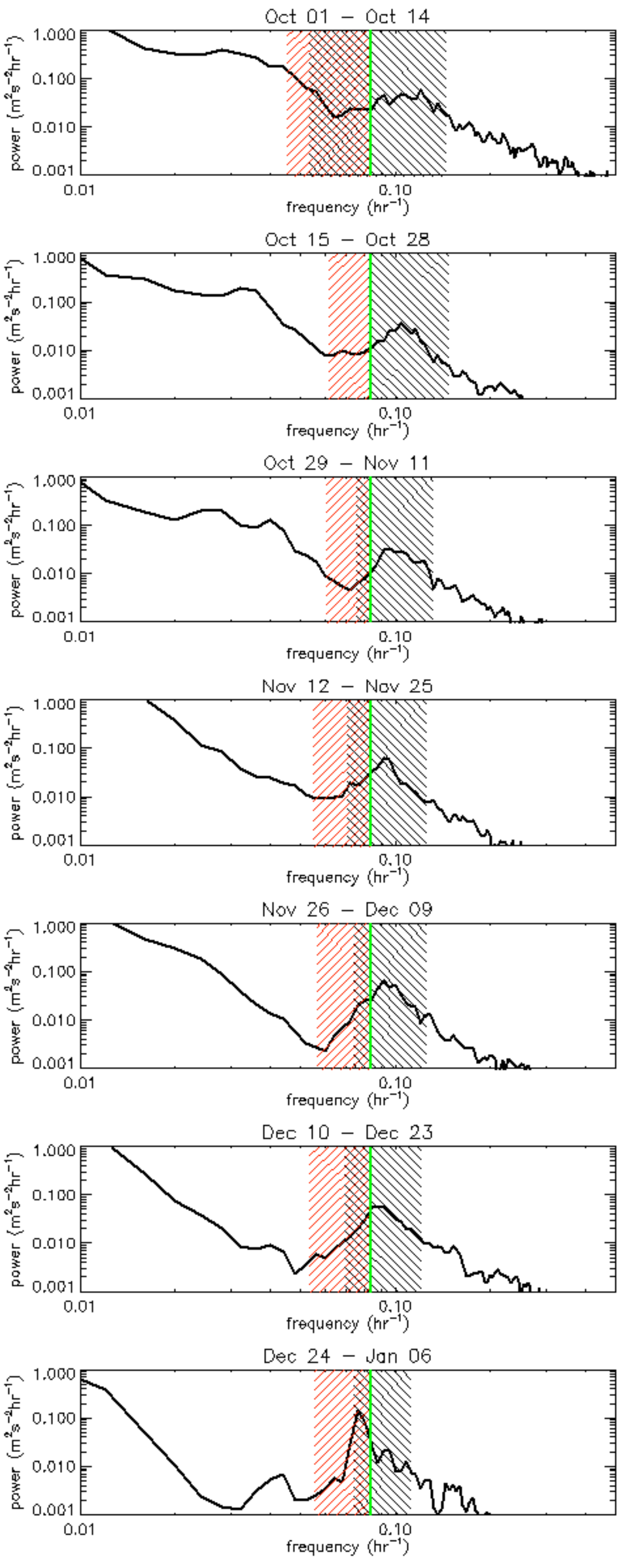
Oct 01 – Oct 14
Oct 15 – Oct 28
Oct 29 – Nov 11
Nov 12 – Nov 25
Nov 26 – Dec 09
Dec 10 – Dec 23
Dec 24 – Jan 06
power ($m^2s^{-2}hr^{-1}$)
1.000
0.100
0.010
0.001
0.01
0.10
frequency (hr^{-1})

Figure 2. Average power spectra from Fourier analysis of zonal winds. Each panel shows the average of individual balloon spectra in a 2-week period (black line). The red-hatched region shows the range of inertial frequencies f for all balloons in flight during the 2-week window. The black-hatched region shows the range of absolute vorticity $\bar{\zeta}_a$ in each two-week period. The green line indicates the semidiurnal tide, which appears in mid-November.

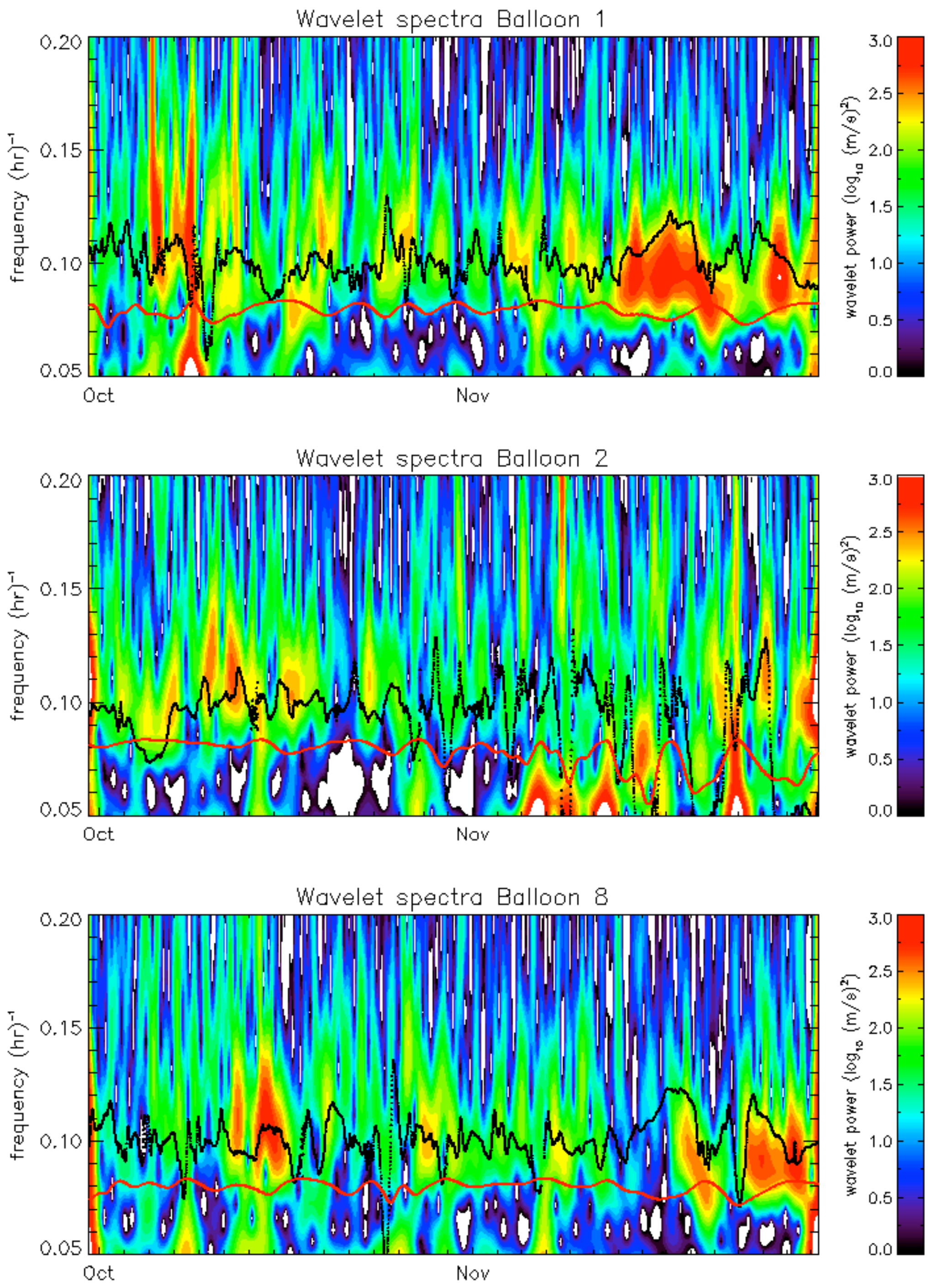

Figure 3. Wavelet spectra for balloons 1, 2 and 8, released near 50 hPa. Inertial frequency *f* (a function only of latitude) is shown in red for each balloon trajectory. The

absolute vorticity (a function of latitude and relative vorticity) is shown as a solid black line.

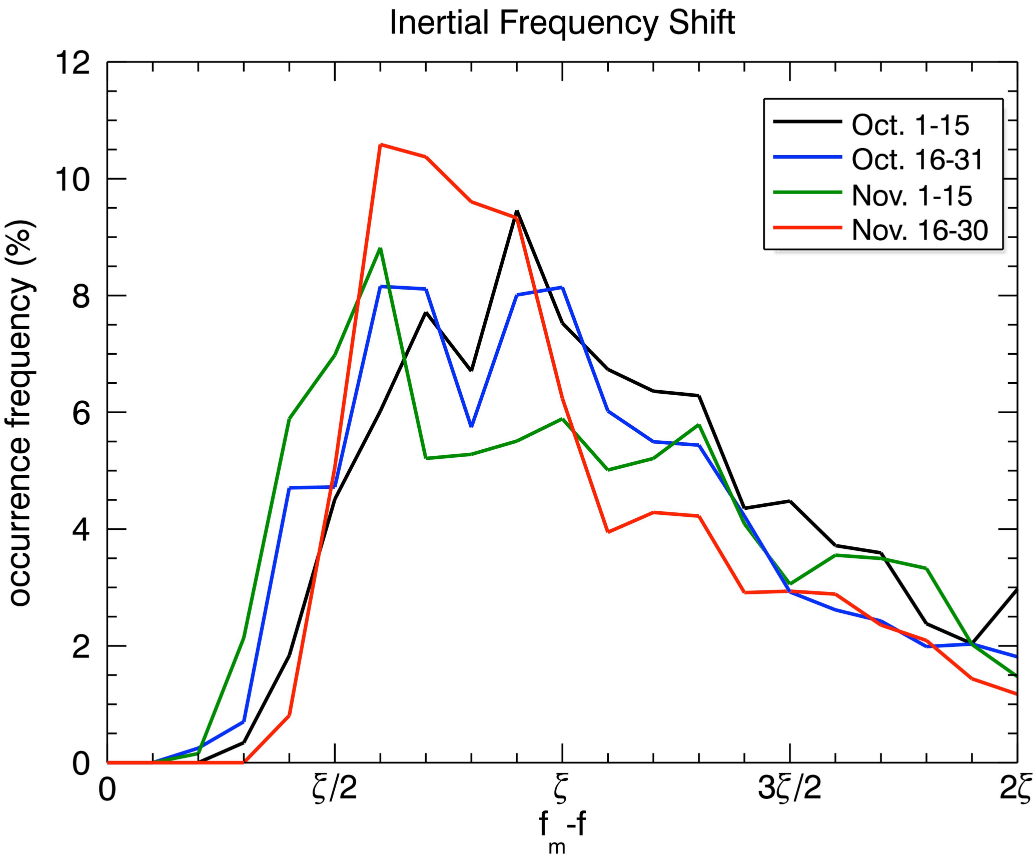

Figure 4. Statistical analysis of the occurrence frequency of inferred differences between the frequency of the measured spectral peak (f_m) and the inertial frequency (*f*). Values are shown for successive two-week periods in October and November. Peaks are observed near $\overline{\zeta}_a = f + \overline{\zeta}$ and between $\overline{\zeta}_a$ and $\overline{\zeta}_a \pm \overline{\zeta}/2$.

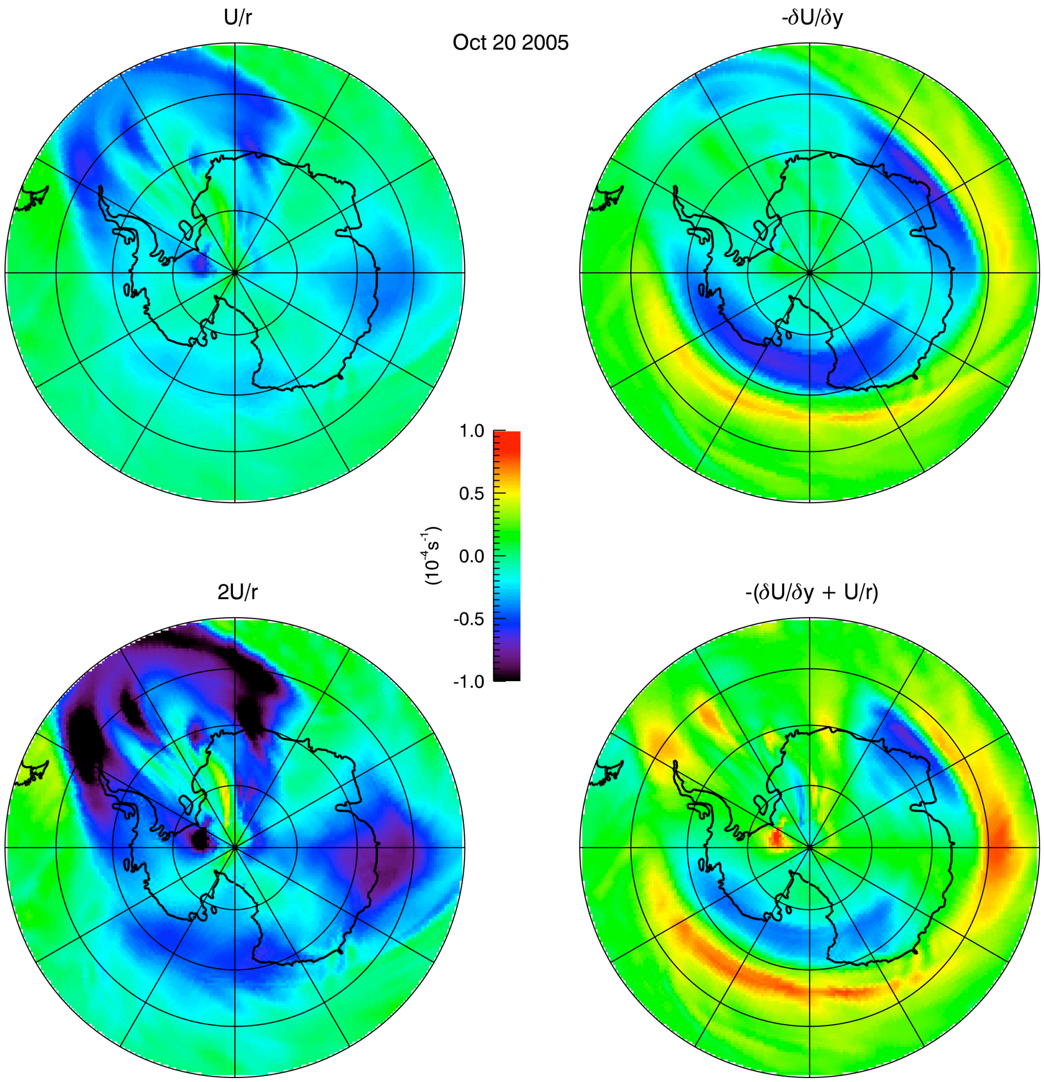

Figure 5. The top two panels show maps of the curvature and shear vorticity, U/r and $\partial U/\partial y$, respectively (see text). The contribution from solid body rotation $2U/r$ is shown in the lower left panel and the non-solid body shear vorticity $-\left(\partial U/\partial y + U/r\right)$ defined in (13) is shown in the lower right panel.

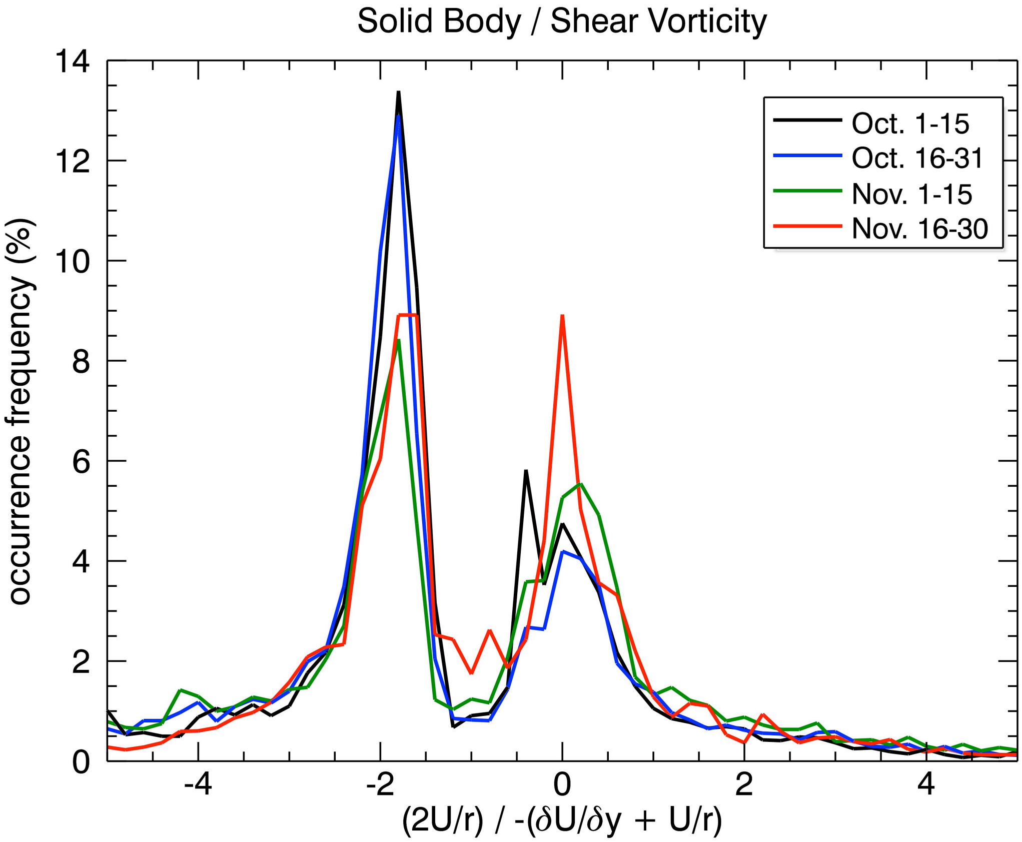

Figure 6. Statistical analysis of the occurrence frequency of the solid body to shear ratio for each two-week period of balloon measurements (See Figure 4).